

# Al<sub>2</sub>B<sub>2</sub> and AlB<sub>4</sub> monolayers: emergence of multiple two-dimensional Dirac nodal line semimetals with novel properties

Saeid Abedi,<sup>1</sup> Esmail Taghizadeh Sisakht,<sup>1,\*</sup> S. Javad Hashemifar,<sup>1</sup> Nima Ghafari Cherati,<sup>1</sup> Ismaeil Abdolhosseini Sarsari,<sup>1</sup> and Francois M. Peeters<sup>2</sup>

<sup>1</sup>*Department of Physics, Isfahan University of Technology, Isfahan, 84156-83111, Iran*

<sup>2</sup>*Department of Physics, University of Antwerp, Groenenborgerlaan 171, B-2020 Antwerpen, Belgium*

(Dated: October 19, 2021)

Topological semimetal phases in two-dimensional (2D) materials have gained widespread interest due to their potential applications in developing nanoscale devices. Despite the prediction of the Dirac/Weyl points in a wide variety of 2D candidates, materials featuring topological nodal lines are still in great scarcity. Herein, we predict two stable thinnest films of aluminum diboride with hyper- and hypo-stoichiometries of Al<sub>2</sub>B<sub>2</sub> and AlB<sub>4</sub> as new 2D nonmagnetic Dirac nodal line semimetals (NLSMs) which promise to offer many novel features. Our elaborate electronic structure calculations combined with analytical studies reveal that, in addition to the multiple Dirac points, these 2D configurations host various type-I closed nodal lines (NLs) around the Fermi level, all of which are semimetal states protected by the time-reversal and in-plane mirror symmetries. The most intriguing NL in Al<sub>2</sub>B<sub>2</sub> encloses the K point and crosses the Fermi level with a considerable dispersion, thus providing a fresh playground to explore exotic properties in dispersive Dirac nodal lines. More strikingly, in the case of 2D superconductor AlB<sub>4</sub> which exhibits a high transition temperature, we provide the first evidence for a set of 2D nonmagnetic open type-II NLs in weak spin-orbit coupling limit, coinciding with closed type-I NLs near the Fermi level. The coexistence of superconductivity and nontrivial band topology in AlB<sub>4</sub> not only makes it a promising material to exhibit novel topological superconducting phases, but also the rather large energy dispersion of type-II nodal lines in this configuration, may offer a distinguished platform for realization of novel topological features in two-dimensional limit.

Topological classification of quantum states of matter has provided a new paradigm for the study of modern condensed matter physics. This vibrant area of research has emerged thanks to the discovery of two- (2D) and three-dimensional (3D) topological insulators (TIs) [1–6]. TIs are insulating in bulk, while host conducting edge/surface states at the boundary that are protected by the time-reversal (TR) symmetry. Beyond the topological insulating phase, a new class of topological materials is realized that exhibit a gapless bulk band structure and thus called topological semimetals (TSMs) or topological metals [7–11].

TSMs are characterized by the key features of the band crossing originated from the crystal symmetries. Depending on the type of band degeneracy, the codimension, and the band dispersion, one can categorize TSMs into three general classes of nodal Dirac/Weyl points [12–18], nodal lines (NLs) [19–27], and nodal surfaces [28–32]. The first class includes Dirac/Weyl semimetals where the band crossings are isolated points with four-fold/two-fold degeneracy and the quasi-particle excitations disperse linearly and obey the Dirac/Weyl equations. In the second class, degenerate dispersive lines appear either as an open or a closed nodal line across the Brillouin Zone (BZ) and are divided into type-I, type-II, and hybrid topological NLs [33]. The third class of TSMs involve band crossings that form a nodal surface in the BZ [28–32, 34].

Recent developments in the realization of 2D topo-

logical materials will pave the way for studying exotic quantum phenomena at the nanoscale that might lead to novel quantum devices. 2D NLSMs are new members of this family that have been the focus of attention in recent studies. Besides the important properties of these systems including non-dispersive Landau energy levels [35], high-temperature surface superconductivity [36], and specific long-range Coulomb interactions [37], one of the most notable characteristics of 2D NLSMs is that their topological features can be revealed by the angle-resolved photoemission spectroscopy (ARPES) measurements [38]. In spite of the large number of discovered 3D TSMs, there are a limited number of 2D materials exhibiting NLSMs [38–42]. Some examples include 2D Lieb lattice [43, 44], monolayer borophene [45], honeycomb-Kagome lattice [46], transition metal chalcogenide monolayers [39], Cu<sub>2</sub>Si [47], and CuSe [48] monolayers, where the two last cases are experimentally realized. Therefore, the exploration of new 2D NLSM materials is of great interest.

The bulk structure of AlB<sub>2</sub>-type materials are known to be 3D TSMs and exhibit specific properties including superconductivity in MgB<sub>2</sub> [49] and ZrB<sub>2</sub> [50], excellent thermoelectricity in AlB<sub>2</sub> [51] and MgB<sub>2</sub> [52], and super-hardness in OsB<sub>2</sub> [53]. Moreover, novel topological states including triple point, nexus, and nodal links has been verified experimentally and theoretically in TiB<sub>2</sub> and ZrB<sub>2</sub> [24–26, 54, 55], where, the dominant features of the energy bands near the crossing points come from the Ti- and Zr-3d states and the appeared NLs are protected by mirror reflection symmetries [24, 25]. Alternatively,

\* taghizadeh.sisakht@gmail.com

a topological Dirac nodal line (DNL), dispersed along the K-H direction and protected by the combination of inversion and TR symmetries [56], has been observed in the conventional high-temperature superconductor  $\text{MgB}_2$  and its non-superconducting sister  $\text{AlB}_2$  [56, 57]. In contrast to  $\text{TiB}_2$  and  $\text{ZrB}_2$ , the DNLs in  $\text{AlB}_2$  and  $\text{MgB}_2$  originate from the B-2p electrons. As a result, the spin-orbit coupling (SOC) in these materials is negligible and consequently the involved topological nodal lines are experimentally feasible [57].

It has been shown that the mechanical cleavage of  $\text{AlB}_2$  flakes may lead to highly single-crystalline 2D layers of this material [58]. In addition, recent ARPES measurements on a typical cleaved (001) surface of  $\text{AlB}_2$  revealed the feasibility of both B- and Al-terminations [59]. In a similar work, a B-terminated monolayer of  $\text{AlB}_2$  was successfully synthesized on Al(111) via molecular beam epitaxy [60]. These experimental works, evidence the feasibility of aluminum diboride thin films with the desired terminations. Herein, we study three atomic layers  $\text{AlB}_2$  thin films with the Al- and B- terminations, leading to the  $\text{Al}_2\text{B}_2$  and  $\text{AlB}_4$  stoichiometries, by using the first-principles calculations, group theory analyses and effective Hamiltonian models (including WTB and continuum models).

After confirmation of the structural stability of these compounds, we investigate the topological aspects of the characteristic band structures. Then, we present a thorough group theory analysis to explain the protection mechanism behind the emergence of various Dirac points and NLs. Meanwhile, we also provide effective continuum models using the *method of invariants* [61] to systematically reproduce the momentum distribution of DNLs and responsible low-energy band dispersions around these Dirac nodes. Our results indicate that there exist several type-I 2D NLs in a relatively small energy range around the Fermi levels of  $\text{Al}_2\text{B}_2$  and  $\text{AlB}_4$  which enclose high symmetry points in the BZ. Very interestingly, for the  $\text{Al}_2\text{B}_2$  configuration there is an NL that encloses the K point and crosses the Fermi level with a dispersion of  $\sim 0.6$  eV. Most strikingly, we realize the coexistence of an open type-II 2D nodal line with other Dirac nodal features in  $\text{AlB}_4$  configuration which arises from the intersection of those energy bands that contributes to determining the superconducting behavior in this material. Our predictions not only enrich the family of 2D NLSMs, but also highlight the potential of these topological materials as promising candidates to explore exotic properties in dispersive 2D Dirac nodal lines and the interplay of the superconductivity and topological Dirac nodal line states [62].

## Results and discussion

**Crystal structures and phonon dispersions.** Depending on the (001) surface termination, one may consider two configurations for the thinnest  $\text{AlB}_2$  films with the in-plane mirror symmetry, which is crucial for the emergence of nodal line in the system. Figure 1(a) shows the similar top view of these two configurations where

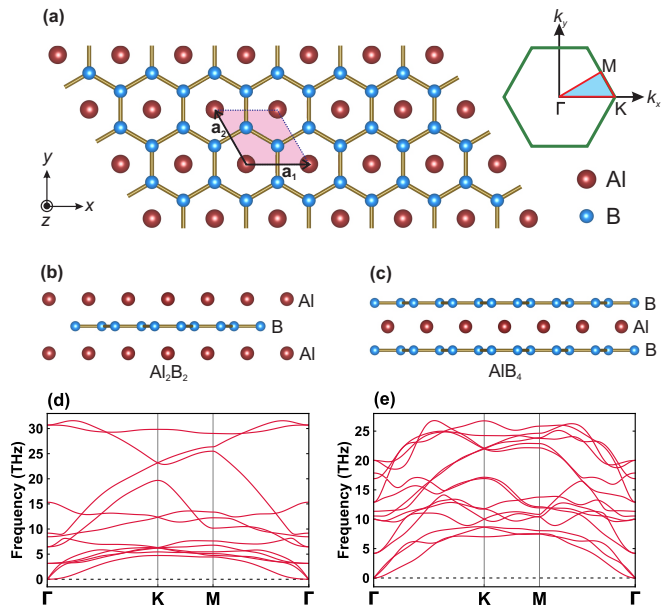


FIG. 1. (a) Top view and BZ of aluminum diboride thin films with lattice vectors  $\mathbf{a}_1$  and  $\mathbf{a}_2$ . (b) and (c) Side views of thinnest films of Al-B<sub>2</sub>-Al and B<sub>2</sub>-Al-B<sub>2</sub> configurations. (d) and (e) Phonon frequencies of  $\text{Al}_2\text{B}_2$  and  $\text{AlB}_4$ .

the lattice vectors  $\mathbf{a}_1$  and  $\mathbf{a}_2$  indicate their surface unit cells. The first pattern of the atomic layers lies within the hypo-stoichiometric  $\text{Al}_{1+x}\text{B}_2$  films and consists of a boron layer intercalated between two aluminum layers with the Al-B<sub>2</sub>-Al stacking (Fig. 1(b)). The second one is the thinnest hyper-stoichiometric  $\text{AlB}_{2+x}$  film with a sandwich B<sub>2</sub>-Al-B<sub>2</sub> configuration (Fig. 1(c)), where the two boron layers form an AA-stacking order enclosing a triangular aluminum layer. The crystal structure of our hypo- and hyper-stoichiometric thin films, referred to as  $\text{Al}_2\text{B}_2$  and  $\text{AlB}_4$ , respectively, belongs to the layer group  $P6/mmm$  (No.80) with the corresponding point group  $D_{6h}$  [63]. Our structural optimizations lead to the in-plane lattice constants 2.994 Å and 2.949 Å for the  $\text{AlB}_4$  and  $\text{Al}_2\text{B}_2$  films, respectively. To evaluate the dynamic stability of these structures, we calculated and considered their phonon spectra. The obtained phonon band structures, presented in Figs.1(d) and (e), clearly indicate absence of any imaginary phonon mode, thus implying their dynamical stability.

Having established the stability of these configurations, we now turn our attention to the electronic and topological properties. As both the  $\text{AlB}_4$  and  $\text{Al}_2\text{B}_2$  structures are composed of light elements, the SOC is quite weak in these materials and one would expect to observe a definite sign of possible Dirac features in experimental measurements. Therefore, we shall ignore the spin of electrons throughout our calculations.

**DNLs in  $\text{Al}_2\text{B}_2$ .** We begin by investigating the electronic and topological properties of  $\text{Al}_2\text{B}_2$  configuration. As mentioned before, the point group of this structure is  $D_{6h}$  which contains 24 symmetry elements. We have

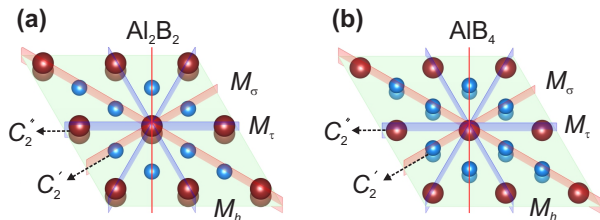


FIG. 2. Three types of mirror planes  $M_\sigma$ ,  $M_\tau$ , and  $M_h$  for (a)  $\text{Al}_2\text{B}_2$  and (b)  $\text{AlB}_4$  configurations, as indicated by the red, blue, and green planes, respectively. Two of rotational axes  $C_2'$  and  $C_2''$  are shown by dashed arrows.

shown in Fig. 2(a) those symmetry elements that are important for our purpose. They are the two different sets of twofold symmetry axes ( $3C_2'$  and  $3C_2''$ ), two different sets of vertical mirror planes ( $3M_\sigma$  and  $3M_\tau$ ), and one horizontal symmetry plane ( $M_h$ ). Figure 3(a) depicts the electronic band structure of  $\text{Al}_2\text{B}_2$  along the highly symmetric directions (M-K- $\Gamma$ -M) in the BZ. As seen from Figs. 3(b) and (c), the atom-projected and orbital-projected bands show that the metallicity of  $\text{Al}_2\text{B}_2$  comes from the hybridization among  $s$  and  $p$  electron valence shells of both Al and B atoms. Interestingly, in the energy range from -2.4 to 1.2 eV, we find multiple band crossing features (consisting of Dirac points (DPs) and nodal points (NPs)) that offer a fruitful line of investigation for 2D topological NLs in this configuration. A close inspection of the band structure reveals that in this energy window there exist two Dirac points and five type-I 2D NLs. We mark the two Dirac points as DP1 and DP2 and indicate the nodal points as  $\text{NP}_i$  and  $\text{NP}_i'$  ( $i$  runs from 1 to 5) that are the pertinent points in the nodal loop  $\text{NL}_i$  (see Fig. 3(a)). The formation of multiple topological nodal loops and Dirac fermions in this band structure suggests that the understanding of the mechanism behind it has to be questioned. Therefore, what follows is a discussion to demystify the reason for the observation of the introduced 2D NLs and Dirac points utilizing the group theory analysis, TB approximation, and method of invariants. First of all, to gain a better insight into the band structure of monolayer  $\text{Al}_2\text{B}_2$  in the whole BZ, we have constructed a TB Hamiltonian in the basis of maximally localized Wannier functions. The comparison of the band structures of  $\text{Al}_2\text{B}_2$  as calculated by density functional theory (DFT) and the WTB Hamiltonian is shown in Fig. 4. One can see that in the mentioned energy range the Wannier band structure exactly matches the DFT results. Next, we have diagonalized our Hamiltonian in the whole BZ to provide the 3D energy bands whose intersections form the mentioned 2D DNLs. Figures 5(a)-(d) depict zoomed-in band structures in the regions of band crossing near nodal points  $\text{NP}_i$  and  $\text{NP}_i'$  (see top views in Figs. 5(e)-(h)). From the transparent top views of bands surfaces, it is clear that the two points  $\text{NP}_i$  and  $\text{NP}_i'$  are residing on a 2D nodal loop  $\text{NL}_i$ . The extensions of nodal points are displayed throughout 3D energy-momentum spaces which vividly describe the

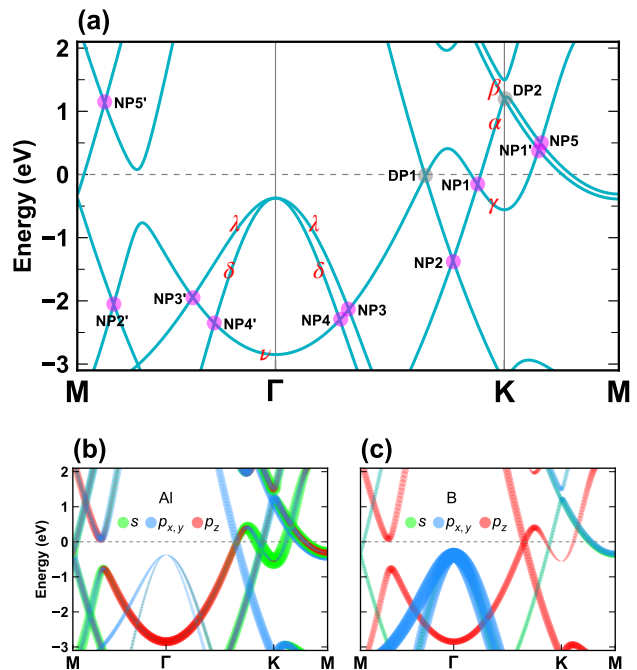


FIG. 3. (a) The calculated electronic band structure of  $\text{Al}_2\text{B}_2$  configuration. Energy dispersion display multiple band crossing features including both Dirac and nodal points as presented by magenta circles. Special bands are marked by Greek letters. (b) and (c) Atom-projected band structures for  $\text{Al}_2\text{B}_2$  contributed by Al and B atoms, respectively. The size of dots is proportional to the weight of contributed orbitals.

form of characteristic topology of each NL. As seen,  $\text{NL}_1$  and  $\text{NL}_5$  surround the K and M points, respectively and  $\text{NL}_2$ ,  $\text{NL}_3$ , and  $\text{NL}_4$  are three concentric nodal loops centered around the  $\Gamma$  point. These Dirac nodal loops have dispersion at different energy levels in the BZ such that cover a large portion of the mentioned energy window. Let us now turn to the mechanism by which the Dirac points DP1 and DP2 emerge. As shown in Fig. 3(a), the DP1 point is located along the  $\Gamma$ -K direction and 25 meV below the Fermi level. The little group for  $\text{Al}_2\text{B}_2$  configuration along this high symmetry direction is  $C_{2v}$  with two perpendicular mirror reflections planes;  $M_\tau$  and  $M_h$  which their intersection introduces the twofold rotation axis  $C_2$ . Our symmetry analysis shows that the irreducible representations (IRs) of the crossing bands around the DP1 point are  $\Gamma_3$  and  $\Gamma_4$  (Fig. 4). Since the IRs  $\Gamma_3$  and  $\Gamma_4$  under the  $M_\tau$  or  $C_2$  symmetry operation have opposite parities, the two bands around the DP1 point do not interact. As a result, six symmetry protected Dirac points DP1 emerge in the whole BZ due to the star of  $k$ . The Dirac point DP2 with an n-type character is located at the K point which stems from the underlying point group  $D_{6h}$  of the lattice in a similar manner to the formation of Dirac cones in graphene. We now begin to consider the mechanism which generates  $\text{NL}_1$ . An important feature of this nodal line is that

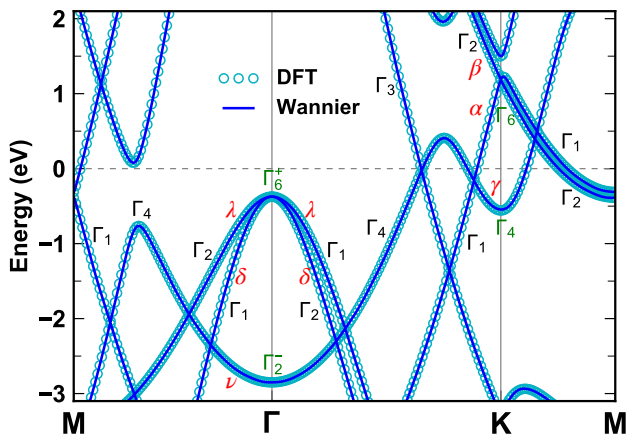


FIG. 4. Comparison of the band structures of  $\text{Al}_2\text{B}_2$  along highly symmetric directions as calculated by DFT and the WTB Hamiltonian. The Wannier band structure exactly matches the DFT results. The IRs of energy bands along these symmetry paths and at high symmetry points K and  $\Gamma$  are also shown.

it crosses the Fermi level and disperses from about  $-0.2$  to  $+0.4$  eV (see Fig. 3(a)). For more convenience, in the vicinity of the nodal points NP1 and NP1' we label the responsible electronic bands as  $\alpha$ ,  $\beta$ , and  $\gamma$ . As seen from Figs. 3(b) and (c), the electronic states of these bands near the Fermi level in the vicinity of the nodal points NP1 and NP1' are mainly decided by Al-s and Al- $p_{x,y}$ . Similar to the  $\Gamma$ -K path, the little group along the K-M direction is also  $C_{2v}$  with the mentioned symmetry operations. Group theory analysis shows that the  $\alpha$ ,  $\beta$ , and  $\gamma$  bands belong to three different  $\Gamma_1$ ,  $\Gamma_2$  and  $\Gamma_4$  IRs, respectively (Fig. 4). Along the  $\Gamma$ -K direction, the  $\alpha$  and  $\gamma$  bands have opposite eigenvalues either with respect to  $C_2$  or  $M_h$  symmetry operations. These opposite parities ensure the decoupling of the  $\alpha$  and  $\gamma$  bands leading to the formation of topologically protected NP1. On the other hand, along the symmetry line K-M, the opposite parities of  $\beta$  and  $\gamma$  bands under either  $M_\tau$  or  $M_h$  operations allow the emergence of topological point NP1'. Besides the justification of the two nodal points NP1 and NP1' along high-symmetry paths, we also examine the mechanism of the other touching points in the NL1. Figure 6 illustrates the band structure of  $\text{Al}_2\text{B}_2$  along a typical low-symmetry line X-K where X is a point between the  $\Gamma$  and M points. Due to the mirror reflection symmetry  $M_h$  of monolayer  $\text{Al}_2\text{B}_2$ , we found that the little group of the X-K line is  $C_s$  and the two crossing bands near the Fermi level belong to different IRs  $\Gamma_1$  and  $\Gamma_2$  as marked in Fig. 6(a). This is valid for the set of the mentioned typical paths. These different representations have opposite parities with respect to  $M_h$ , giving rise to a distribution of touching points that construct the 2D topological NL1 (see Figs. 5(a) and (e)).

To further analyze the structure of NL1 and the corresponding crossing bands, we use group theory to derive a matrix Hamiltonian with invariant expansion

method [61] which describes the electron states in the vicinity of the K point. This method enables us to systematically incorporate the allowed terms up to any desired order of wave vector  $\mathbf{k}$ . The little group of the wave vector K in  $\text{Al}_2\text{B}_2$  is  $D_{3h}$ . At this point the two degenerate Bloch states of the  $\alpha$  and  $\beta$  bands transform according to the 2D IR  $\Gamma_6$  as denoted by  $\psi^\alpha$  and  $\psi^\beta$ , while the corresponding wave function of the  $\gamma$  band ( $\psi^\gamma$ ) transforms as IR  $\Gamma_4$ . These basis functions allow us to construct the  $3 \times 3$  matrix Hamiltonian  $\mathcal{H}^K$  around the K point which falls into four blocks

$$\mathcal{H}^K = \begin{pmatrix} \mathcal{H}_{11} & \mathcal{H}_{12} \\ \mathcal{H}_{21} & \mathcal{H}_{22} \end{pmatrix}, \quad (1)$$

where each block  $\mathcal{H}_{ij}$  has a dimension of  $n_i \times n_j$  and  $n_i$  ( $n_j$ ) denotes the dimension of representation  $\Gamma_i$  ( $\Gamma_j$ ). The diagonal blocks  $\mathcal{H}_{11}$  ( $2 \times 2$ ) and  $\mathcal{H}_{22}$  ( $1 \times 1$ ) describe energy bands that transform according to the IRs  $\Gamma_6$  and  $\Gamma_4$ , respectively. Each block  $\mathcal{H}_{ij}$  depends on a tensor operator  $\mathcal{K}$  which represents a function of the components of the wave vector  $\mathbf{k}$ . Bir and Pikus [61] showed that for a symmetry element  $g$  with matrix representation  $\mathcal{D}(g)$ , the invariance condition

$$\mathcal{D}(g) \mathcal{H}(g^{-1}\mathcal{K}) \mathcal{D}^{-1}(g) = \mathcal{H}(\mathcal{K}), \quad (2)$$

leads to the general form  $\mathcal{H}_{ij}$  as

$$\mathcal{H}_{ij}(\mathcal{K}) = \sum_{\kappa, \nu} a_{\kappa\nu}^{ij} \sum_{l=1}^{d_\kappa} X_l^{(\kappa, ij)} \mathcal{K}_l^{(\kappa, \nu)*}. \quad (3)$$

The parameters  $a_{\kappa\nu}^{ij}$  are material-dependent constants which can be determined via a fitting procedure.  $X_l^{(\kappa, ij)}$  are those linearly independent  $n_i \times n_j$ -dimensional basis matrices that transform as those irreducible representations  $\Gamma_\kappa$  which occurs in the product  $\Gamma_i \times \Gamma_j^*$ . Here,  $l$  denotes the  $l$ th basis matrix and runs up to  $d_\kappa$ , the dimension of representations  $\Gamma_\kappa$ . Also,  $\mathcal{K}_l^{(\kappa, \nu)}$  are the  $l$ th component of the  $\nu$ th-order of the tensor operator  $\mathcal{K}$  which transform in a similar way. To construct the basis matrices  $X_l^{(\kappa, ij)}$  and an arbitrary order of the tensor operators  $\mathcal{K}_l^{(\kappa, \nu)}$ , one can utilize Clebsch-Gordan coefficients which have been tabulated in Ref. [64]. The construction procedure of these matrices- and tensor-components has been described in Refs. [65, 66].

Besides the invariance condition (2), the TR symmetry of the system also imposes an additional constraint on the diagonal blocks  $\mathcal{H}_{ii}$  [66]. Therefore, when using the invariant method to construct the effective Hamiltonians, we will additionally consider this constraint to list the allowed tensor-components  $\mathcal{K}_l^{(\kappa, \nu)}$ .

Let us now proceed by generating the clear form of the Hamiltonian  $\mathcal{H}^K$  up to second order in  $\mathbf{k}$  components using the introduced method. As mentioned, around the K point the Bloch functions  $\psi^\alpha$  and  $\psi^\beta$  transform according to the IR  $\Gamma_6$  of  $D_{3h}$ . Also, the Bloch function  $\psi^\gamma$  transforms as representation  $\Gamma_4$ . Therefore, from a group theoretical point of view, one may adopt  $\{x - iy, x + iy\}$  and



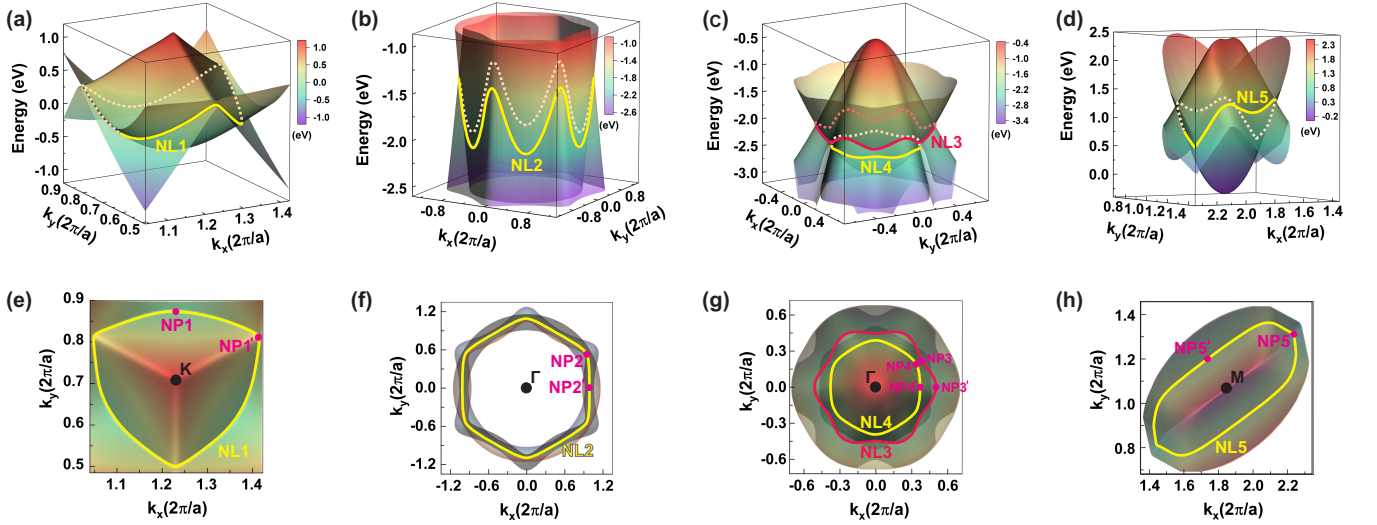


FIG. 5. (a)-(d) 3D visualizations of energy bands obtained from  $\text{Al}_2\text{B}_2$  WTB Hamiltonian. Bands whose crossings lead to the formation of nodal lines around the K,  $\Gamma$ , and M points are shown. The extensions of nodal lines can be seen vividly throughout 3D energy-momentum spaces which form the characteristic topology of each NL. Color bars represent the energy of electrons. (e)-(h) The corresponding top views of (a)-(d). The momentum distributions of gapless nodal points are shown. Note that in Figs.(b) and (f) some data values were removed for better visualization.

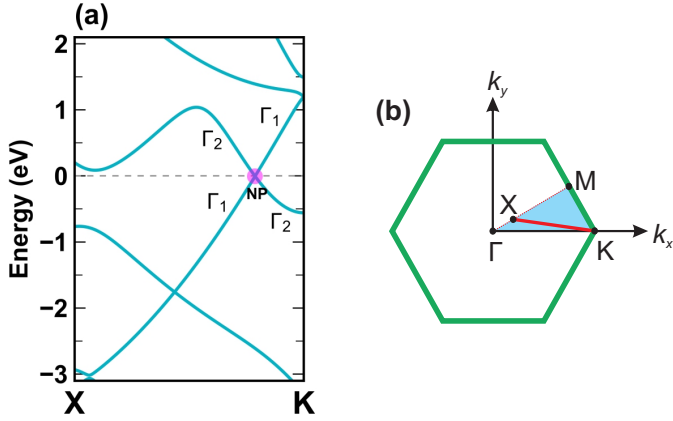


FIG. 6. (a) Electronic band structure of  $\text{Al}_2\text{B}_2$  along the typical low-symmetry path X- $\Gamma$  in the BZ as shown in (b).

$\{z\}$  as basis functions to obtain the basis matrices  $X_l^{(\kappa,ij)}$ . Choosing this set of basis functions, we obtained the basis matrices as listed in Table S1 (see Supplementary Note 1). Likewise, we can obtain the irreducible tensor components up to  $k_i k_j$  terms that transform accordingly and are allowed by TR invariance. According to Herring's rule, considering the TR symmetry may lead to three different possibilities 'a', 'b', and 'c' for a spinless system [67]. In case 'a', no additional degeneracies occur by applying the TR operator. However, when the two inequivalent wave vectors  $\mathbf{k}$  and  $-\mathbf{k}$  are related via a symmetry element  $R$  (known as case 'a<sub>2</sub>'), one needs to consider the additional condition [61]

$$\mathcal{T}^{-1}\mathcal{H}(R^{-1}\mathcal{K})\mathcal{T} = \mathcal{H}^*(f\mathcal{K}) = \mathcal{H}^t(f\mathcal{K}), \quad (4)$$

where  $f = \pm 1$  is the parity of  $\mathcal{K}$  under the TR symmetry. In  $\text{Al}_2\text{B}_2$  the symmetry element  $M_\sigma$  maps the two inequivalent points K and K' onto each other. Choosing the operator  $M_\sigma$ , the TR operator have the form of  $\mathcal{T} = K$  [68], where  $K$  is the complex conjugate operator. Therefore the condition (4) for the K point is written as

$$\mathcal{H}^K(R^{-1}\mathcal{K}) = \mathcal{H}^*(f\mathcal{K}). \quad (5)$$

We have listed in Table S1 those tensor components that satisfy the condition (5). Then, inserting the tabulated symmetrized matrices and tensor components in Eq. (3) we arrive at

$$\mathcal{H}_{11} = [E_0 + Af_1(k)]\mathbb{1} + B(k_x\sigma_x + k_y\sigma_y) + C(f_2(k)\sigma_x + f_3(k)\sigma_y), \quad (6)$$

$$\mathcal{H}_{22} = E'_0 + A'f_1(k), \quad (7)$$

$$\mathcal{H}_{12} = \mathcal{H}_{21} = 0, \quad (8)$$

where we have defined functions  $f_1(k) = k_x^2 + k_y^2$ ,  $f_2(k) = k_y^2 - k_x^2$ , and  $f_3(k) = 2k_x k_y$ . Therefore, the diagonalization of parameter-dependent Hamiltonian (1) results in the three-band energy spectra Eqs. (S1-S2) (see Supplementary Note 1). We then performed a fitting procedure of these energy bands with first-principle data to obtain the numerical values of parameters. The comparison between DFT bands and the bands from our continuous model around the K point is shown in Supplementary Fig.S1. One can see that around this point the fitted bands are in good agreement with the first-principles data. Furthermore, they also reproduce well the band dispersions in 2D BZ (around K point), and therefore the locus of the touching points between these energy bands leads to the emergence of NL1 as depicted

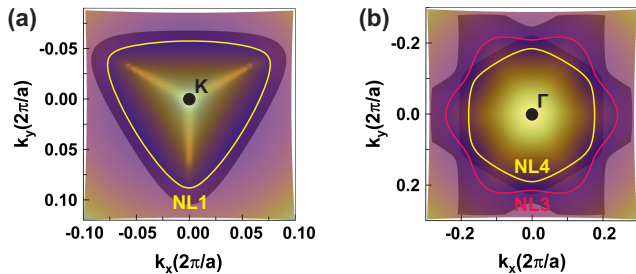


FIG. 7. Transparent top views of crossing bands obtained by continuum model around (a) the K and (b)  $\Gamma$  points of  $\text{Al}_2\text{B}_2$ . The momentum distributions of gapless nodal points (NL1, NL2, and NL3) are reproduced correctly by the continuum model.

in Fig. 7(a).

Having confirmed the existence of NL1 in  $\text{Al}_2\text{B}_2$ , we next study the reasons behind the formation of NL2, NL3, and NL4 which enclose the  $\Gamma$  point. In Fig. 3(a), we observe that all of these nodal lines are located completely below the Fermi level in the range of -2.35 to -1.35 eV which can be revealed by ARPES measurements [38]. Let us first focus on NL3 and NL4 that have distribution near the  $\Gamma$  point. Here, two of the responsible bands are hole-like (labeled as  $\lambda$  and  $\delta$  bands) and the other one is electron-like (labeled as  $\nu$  band). As seen from Figs. 3(b) and (c), the  $\lambda$  and  $\delta$  bands are largely composed of B-p $_{x,y}$  orbitals while the  $\nu$  band is mainly contributed by Al-p $_z$  and B-p $_z$  states. The little group of wave vectors  $\mathbf{k}$  along the  $\Gamma$ -M direction with symmetry elements  $E$ ,  $C_2$ ,  $M_\sigma$ , and  $M_h$  shares the same point group symmetry as  $\Gamma$ -K and K-M paths. Therefore, the energy bands of  $\text{Al}_2\text{B}_2$  along this direction belong to one of the irreducible representations of the  $C_{2v}$  point group. As shown in Fig. 4, a symmetry analysis unveils that along  $\Gamma$ -K ( $\Gamma$ -M) directions the  $\lambda$ ,  $\delta$ , and  $\nu$  bands belong to three different 1D irreducible representations  $\Gamma_1(\Gamma_2)$ ,  $\Gamma_2(\Gamma_1)$ , and  $\Gamma_4$ , respectively. For both symmetry directions, the corresponding bands with different IRs  $\Gamma_1$  and  $\Gamma_4$  have opposite parities with respect to either  $C_2$  or  $M_h$  symmetry elements. Therefore, they will not hybridize with each other, allowing them to meet at NP3 and NP4'. Similarly, for symmetry direction  $\Gamma$ -K ( $\Gamma$ -M), the energy bands with IRs  $\Gamma_2$  and  $\Gamma_4$  have opposite parities under mirror symmetries  $M_h$  or  $M_\tau$  ( $M_\sigma$ ), leading to the formation of the nodal point NP4 (NP3'). Here, a similar analysis to what we described for the formation of NL1 could be applied to confirm that no gap opens at the crossing between the corresponding bands along a typical low-symmetry line X- $\Gamma$ , leading to the emergence of NL3 and NL4.

We now turn to the method of invariants. This approach also provides a good description of momentum distributions of these nodal loops. The little point group at  $\Gamma$  point in the  $\text{Al}_2\text{B}_2$  is  $D_{6h}$ . At this point, the Bloch functions  $\{\psi^\lambda, \psi^\delta\}$  and  $\psi^\nu$  transform according to the IRs  $\Gamma_6^+$  and  $\Gamma_2^-$ , respectively. Taking the set of symmetrical basis functions  $\{x - iy, x + iy\}$  and  $\{z\}$ , we obtained

the basis matrices and the irreducible tensor components that transform accordingly as listed in Supplementary Table S2. Note that at the  $\Gamma$  point we have  $\mathbf{k} = -\mathbf{k} = 0$ . Therefore, according to the Herring test, these irreducible representations belong to the case 'a $_1$ ' [61]. On the other hand, odd functions of  $k_i^n k_j^m$  are not invariants of  $\Gamma_6^+ \otimes \Gamma_6^{+*}$  and  $\Gamma_2^- \otimes \Gamma_2^{-*}$ . As a result, TR invariance implies no additional constraint. Based on these two irreducible representations, we divide the  $3 \times 3$  effective Hamiltonian  $\mathcal{H}^\Gamma$  into four blocks and obtain each block using the method of invariants as follows

$$\mathcal{H}_{11} = [E_0 + Af_1(k)]\mathbb{1} + B[f_2(k)\sigma_x + f_3(k)\sigma_y] + C[f_4(k)\sigma_x + f_5(k)\sigma_y], \quad (9)$$

$$\mathcal{H}_{22} = E'_0 + A'f_1(k), \quad (10)$$

$$\mathcal{H}_{12} = \mathcal{H}_{21} = 0, \quad (11)$$

where  $f_4(k) = k_y^4 - 6k_x^2 k_y^2 + k_x^4$ , and  $f_5(k) = 4(k_x k_y^3 + k_x^3 k_y)$ . The fitting procedure of the eigenvalues of this model with the DFT band structure is presented in Supplementary Fig. S2. Using the fitted values we have shown in Fig. 7(b) a transparent top view of energy bands corresponding to NL3 and NL4, respectively. As seen, our effective Hamiltonian reproduces correctly the hexagon (NL3) and hexagram (NL4) form of the momentum distribution of gapless nodal points.

The other nodal line that we shall examine is NL2. Along the  $\Gamma$ -M direction, the IRs of touching bands at the NP2' point are identical to those of NP4'. Hence, the same group theory analysis is applied to explain the formation of topological nodal point NP2'. On the other hand, along the  $\Gamma$ -K direction, the NP2 nodal point emerges due to the crossing of two energy bands with different IRs  $\Gamma_1$  and  $\Gamma_3$ . Here, the protection of this point is justified by the opposite parity of the two bands under  $M_h$  or  $M_\tau$ . It should be noted that the same interpretation as discussed earlier applies to other touching points of NL2 whose point groups are  $C_s$ .

The remaining nodal line in  $\text{Al}_2\text{B}_2$  is NL5 which encloses the M point. This nodal loop is located at least 0.48 eV above the Fermi energy and is less significant. For this nodal line, along both  $\Gamma$ -M and  $\Gamma$ -K directions the corresponding bands of touching points NP5 and NP5' have the same IRs  $\Gamma_1$  and  $\Gamma_4$ . As the wave functions of these bands have opposite parities under  $C_2$  and  $M_h$ , they prohibit the interaction between them which allow the appearance of these nodal points.

**DNLs in  $\text{AlB}_4$ .** Now that the electronic and topological properties of monolayer  $\text{Al}_2\text{B}_2$  were investigated, we move to examine the case of monolayer  $\text{AlB}_4$ . This configuration share the same symmetry as  $\text{Al}_2\text{B}_2$  with  $D_{6h}$  point group. Figure 2(b) depicts those symmetry elements of  $\text{AlB}_4$  which we are interested in the following. The band structure of  $\text{AlB}_4$  along the highly symmetric paths (M- $\Gamma$ -K-M) is displayed in Fig. 8(a). One can observe from Figs. 8(b) and (c) that around the  $\Gamma$  point and close to the Fermi level energy

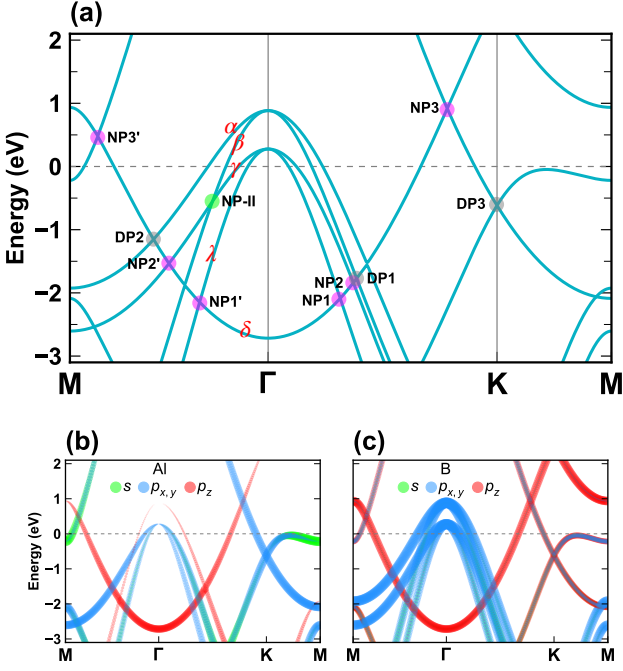


FIG. 8. (a) The calculated electronic band structure of  $\text{Al}_2\text{B}_2$  configuration. Energy dispersion display multiple band crossing features including both Dirac and nodal points as presented by magenta circles. Special bands are marked by Greek letters. (b) and (c) Atom-projected band structures for  $\text{Al}_2\text{B}_2$  contributed by Al and B atoms, respectively. The size of dots is proportional to the weight of contributed orbitals.

bands mainly originate from boron  $\sigma$  orbitals (B-s and B- $p_{x,y}$ ). However, there exist also pure  $\pi$ -bonding boron states as well as mixed orbitals (constructed from B-p, B-s, and Al-s) that cross the Fermi level.

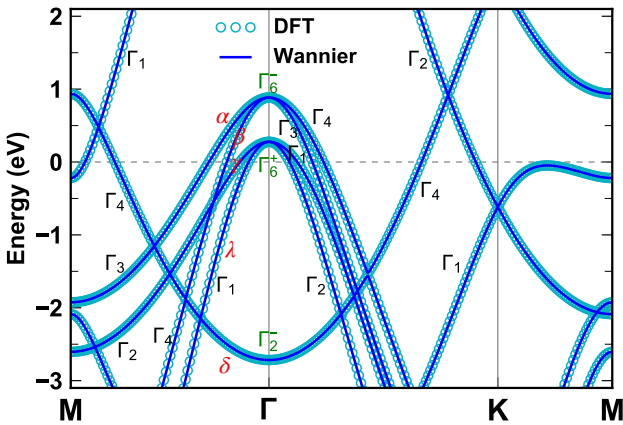


FIG. 9. Comparison of the band structures of  $\text{AlB}_4$  as calculated by DFT and the WTB Hamiltonian. The Wannier band structure exactly matches the DFT results.

In a recent study, the role of these low-energy bands in determining the superconducting behavior of the system has been explored [69]. It was revealed that the

$\text{AlB}_4$  film captures a robust three-gap superconducting nature with a high critical temperature ( $\sim 47$  K) which provides a platform for further investigation of multigap superconductors. Surprisingly, we found that along with the superconducting behavior of these energy bands there are linear band crossing features that emerge as a consequence of lattice symmetries. This led us to investigate the topological aspects of the  $\text{AlB}_4$  band structure which contains several dispersive NLs and Dirac cones.

Let us label the mentioned bands using Greek letters as indicated in Fig. 8(a). In the energy range from -2.2 to 1 eV, the crossing points consist of either nodal points (NPs) or Dirac points (DPs). There are three Dirac points as indicated by DP1 to DP3. Also, the nodal points  $\text{NP}_i$ , and  $\text{NP}_i'$  ( $i$  runs from 1 to 3) are pertinent points which belong to the 2D nodal loop  $\text{NL}_i$ . In addition, there exists a distinct nodal point (NP-II) that corresponds to an open 2D type-II nodal line (NL4). This is to the best of our knowledge the first evidence for the existence of a 2D nonmagnetic open type-II NL in systems at weak SOC limit. Figure 9 shows the comparison of Wannier band structure of  $\text{AlB}_4$  with DFT data. Using the obtained WTB Hamiltonian we provide in Fig. 10 3D energy bands of  $\text{AlB}_4$  near the Fermi level in the vicinity of the  $\Gamma$  point. An inspection of these 3D bands and the corresponding transparent top views (Figs. 10(c) and (d)) reveals that the momentum distribution of type-I nodal loops NL1 and NL3 show a hexagon, while for the other type-I nodal loop i.e. NL2, it is a hexagram. Besides, one can see from Figs. 10(a) and (c) that the open type-II nodal lines NL4 are terminated to the closed nodal hexagram NL2. The coexistence of these two nodal line types which can be confirmed through ARPES [47] or infrared spectroscopy [70] measurements, may provide an ideal platform to study many novel physical properties [71–73] that have been proposed for NLSMs. For example, it is preferred to examine the signatures of Landau levels spectrum collapse [71] on a 2D platform rather than in a 3D material candidate. Also, it might be beneficial to utilize this topological material to explore experimentally the anticipated enhanced correlations in nodal line semimetals [70]. Furthermore, the interplay of the superconductivity and these topological Dirac nodal line states suggests that topological superconducting phases [56] may be realized in this structure which is a subject for further investigations.

The hexagon and hexagram shapes of NL1 (NL3) and NL2 are due to the fact that the underlying symmetries and irreducible representations of the corresponding bands are identical to that of NL4 and NL3 in  $\text{Al}_2\text{B}_2$  lattice, respectively. Therefore, the same group theory and method of invariants analysis applies to explain the formation mechanism of these NLs, and no further discussion seems necessary to highlight here.

Before we turn to the open nodal loop NL4, we shall briefly explain the reasons why Dirac points DP1,

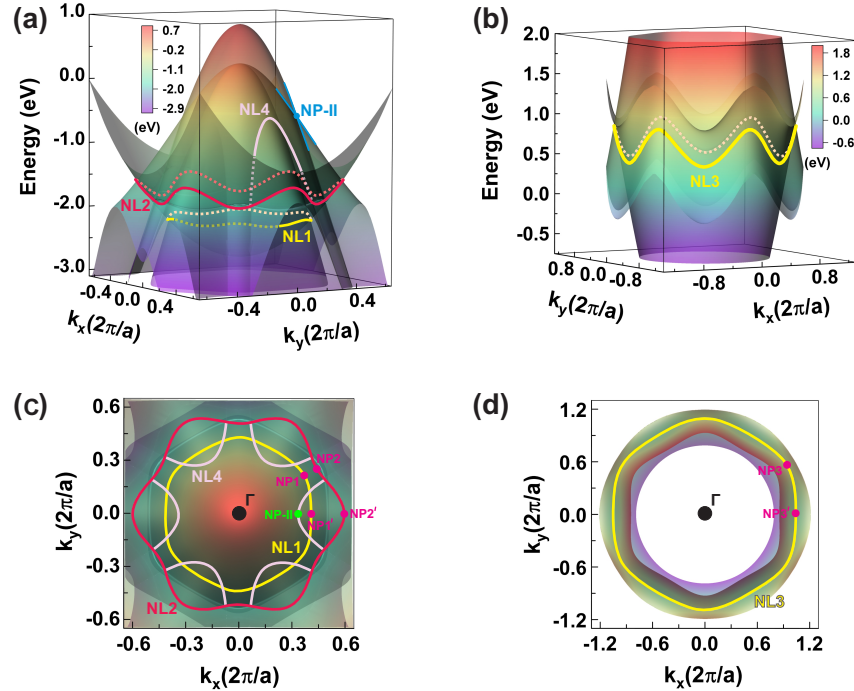


FIG. 10. (a) and (b) 3D visualizations of energy bands obtained from AIB<sub>4</sub> WTB Hamiltonian. Bands whose crossings lead to the formation of nodal lines around the  $\Gamma$  point are shown. The extensions of nodal points can be seen vividly throughout 3D energy-momentum spaces which form the characteristic topology of each NL. Color bars represent the energy of electrons. (c) and (d) The transparent top views of (a) and (b). The momentum distributions of gapless nodal points are shown. Note that in Figs.(b) and (d) some data values were removed for better visualization.

DP2, and DP3 occur in the band structure of this configuration. DP1 and DP2 locate along the  $\Gamma$ -K and  $\Gamma$ -M directions  $\sim 1.18$  eV and  $\sim 1.77$  eV below the Fermi level, respectively. Since the number of such points in the star of  $k$  in the BZ is six, one expect to see the same number of Dirac points. As seen in Fig. 9, the IRs of the touching bands around both Dirac points DP1 and DP2 are  $\Gamma_3$  and  $\Gamma_4$ . Therefore, just similar to the case of DP1 in Al<sub>2</sub>B<sub>2</sub>, the opposite parities of  $C_2$  rotation or mirror  $M_\sigma$  (or  $M_\tau$ ) allow the two bands to touch each other at DP1 and DP2. It is worth mentioning that at first glance, one may expect that similar to a typical point NP $i$ , these points also belong to a nodal line distribution. However, the situation is different here. Along a typical low symmetry X- $\Gamma$  direction with point group  $C_s$ , both bands (around DP1 and DP2) have the same IR  $\Gamma_2$  which prevents them to touch each other, leading to the opening of a gap. The other Dirac point that locates at the K point and  $\sim 0.65$  eV below the Fermi level is DP3 which has the characteristics of the Dirac points in graphene.

Now, we will focus on the topological aspects of type-II nodal line NL4. Along the  $\Gamma$ -M direction, the two electron-like bands  $\beta$  and  $\gamma$  (with the same slope sign) meet  $\sim 0.6$  eV below the Fermi level and show a band crossing as labeled by NP-II (Fig. 8(a)). Figures 11(a) and (b) display band structures of AIB<sub>4</sub> along two typical low-symmetry lines X- $\Gamma$  where X is a point along

the high-symmetry M-K direction (Fig. 11(c)). As seen, for a typical line X1- $\Gamma$ , where X1 is between K and C, there exists no crossing between the  $\beta$  and  $\gamma$  bands. Conversely, when X is between C and M, these two bands crosses along the corresponding X- $\Gamma$  path (Fig.11b). Therefore, the crossing point of the  $\gamma$  and  $\beta$  bands are only distributed in certain Brillouin zone slices, shown in Fig., to form a set of open type-II nodal lines (NL4) in the system. Here, C specifies the low symmetry path wherein NL4 is linked with NL2 (see Fig. 10(c)). The rather large energy dispersion of these type-II nodal lines ( $\sim 1.3$  eV) makes AIB<sub>4</sub> a distinguished 2D candidate for realization of novel topological properties.

The formation of the topologically protected momentum distribution NL4 is justified as follow. Along the high symmetry direction  $\Gamma$ -M with point group  $C_{2v}$ , the IRs of  $\beta$  and  $\gamma$  bands are  $\Gamma_4$  and  $\Gamma_2$ , respectively (see Fig. 9). The opposite parities of these two bands under mirror symmetries  $M_h$  or  $M_\sigma$  decouple the associated electronic states and allow the formation of the nodal point NP-II. Moreover, along the typical low symmetry line X3- $\Gamma$  with point group  $C_s$ , these bands have different IRs  $\Gamma_2$  and  $\Gamma_1$ . The situation is just similar to the case of NL1 in Al<sub>2</sub>B<sub>2</sub> which permits the appearance of open type-II NL4.

Eventually, using the method of invariants, we derive the effective Hamiltonian model which describes quite well those nodal lines of AIB<sub>4</sub> that locate below the Fermi



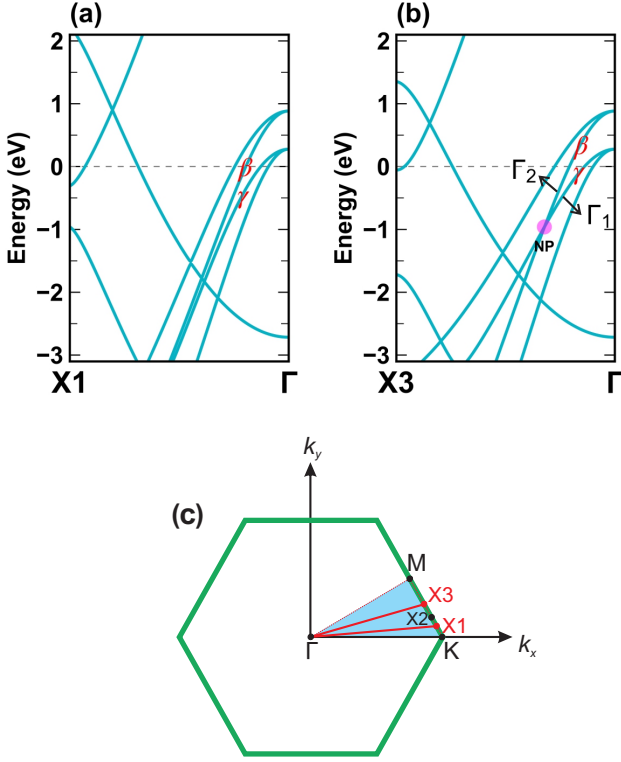


FIG. 11. (a) and (b) Electronic band structures of  $\text{AlB}_4$  along typical low-symmetry paths  $\text{X1-}\Gamma$  and  $\text{X3-}\Gamma$  in the BZ as shown by red lines in (c). The crossing of  $\beta$  and  $\gamma$  bands exists for a typical path  $\text{X-}\Gamma$  where X is located between  $\text{X2}$  and  $\text{M}$  points.

level. For the little group  $D_{6h}$  at  $\Gamma$  point the relevant Bloch states belong to the doubly degenerate IRs  $\Gamma_6^-$ ,  $\Gamma_6^+$ , and nondegenerate IR  $\Gamma_2^-$  as shown in Fig. 9. Thus, the corresponding Bloch functions allow us to construct an effective  $5 \times 5$  block diagonal Hamiltonian  $\mathcal{H}^\Gamma$  around the  $\Gamma$  point as

$$\mathcal{H}^\Gamma = \begin{pmatrix} \mathcal{H}_{11} & \mathcal{H}_{12} & \mathcal{H}_{13} \\ \mathcal{H}_{21} & \mathcal{H}_{22} & \mathcal{H}_{23} \\ \mathcal{H}_{31} & \mathcal{H}_{32} & \mathcal{H}_{33} \end{pmatrix}. \quad (12)$$

Therefore, using the method of invariants we adopt  $\{x - iy, x + iy\}$ ,  $\{x - iy, x + iy\}$ , and  $\{z\}$  as basis functions to obtain the basis matrices as well as tensor components (see [Supplementary Note 3](#)). Inserting the obtained basis matrices and tensor components (TR adds no additional constraint as discussed in the case of  $\text{Al}_2\text{B}_2$ ) in each block of  $\mathcal{H}^\Gamma$  we arrive at

$$\mathcal{H}_{11} = [E_0 + Af_1(k)]\mathbb{1} + B[f_2(k)\sigma_x + f_3(k)\sigma_y] + C[f_4(k)\sigma_x + f_5(k)\sigma_y], \quad (13)$$

$$\mathcal{H}_{22} = [E'_0 + A'f_1(k)]\mathbb{1} + B'[f_2(k)\sigma_x + f_3(k)\sigma_y] + C'[f_4(k)\sigma_x + f_5(k)\sigma_y], \quad (14)$$

$$\mathcal{H}_{33} = E''_0 + A''f_1(k), \quad (15)$$

$$\mathcal{H}_{ij} = 0 \quad i \neq j, \quad (16)$$

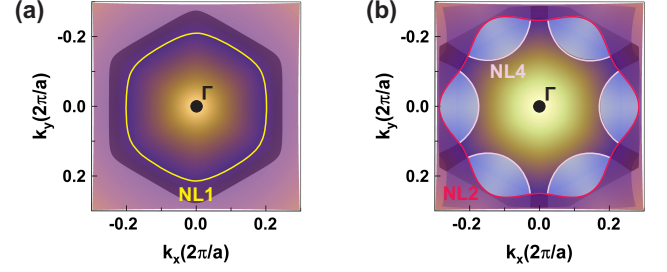


FIG. 12. Transparent top views of crossing bands obtained by continuum model around the  $\Gamma$  point of  $\text{AlB}_4$ . The momentum distributions of gapless nodal lines (a) NL1 and (b) NL2 and NL4 are reproduced correctly by the continuum model.

where we have previously defined  $f_i(k)$  functions. By fitting the parameters with DFT results (see [Supplementary Fig. S3](#)), our continuous five-band model describes very well the formation of open type-II nodal line NL4 as well as NL1 and NL2 around the  $\Gamma$  point as shown in Figs. 12(a) and (b).

Finally, we make some notes on the freestanding monolayer  $\text{AlB}_2$ . Although, group theory analysis of the energy bands unveils that there exist some topologically protected Dirac points along the high symmetry lines in the BZ of this structure, the absence of the in-plane mirror symmetry reduces the point group of the system to  $C_{6v}$  and thus prevents formation of any nodal line feature in the momentum space (See [Supplementary Note 4](#)). It is worth mentioning that the monolayer  $\text{AlB}_2$  with a B-terminated surface has been recently synthesized on  $\text{Al}(111)$  [60] and the existence of the p-type Dirac Fermions in this configuration was confirmed by the recent experimental ARPES measurements [60]. This may serve as a possible way to explore our predicted topological NLSM states in aluminum diborides thin films with in-plane mirrors.

## Summary and conclusions

In summary, using first-principles calculations and group theory analyses, we accurately investigated the electronic structure of  $\text{Al}_2\text{B}_2$  and  $\text{AlB}_4$  thin films to reveal the existence of many nontrivial topological features in these systems. The dynamical stability of these structures was also proven by calculation of their phonon spectra. Our results indicate that the electronic band structures of both configurations host multiple topologically protected band crossings including 2D Dirac nodal lines as well as Dirac points. We then used symmetry analyses to explain the protection mechanism of the nodal lines and then applied the method of invariants to construct proper effective Hamiltonians for systematic investigation of the formation mechanism of these nodal lines. We demonstrated formation of five and three type-I topological NLSMs in the low energy electronic states of the  $\text{Al}_2\text{B}_2$  and  $\text{AlB}_4$  compounds, respectively. It is argued that all of the nodal line states

are protected by the time reversal and in-plane mirror symmetries. In the case of  $\text{Al}_2\text{B}_2$ , three concentric nodal loops sit below the Fermi level and surround the  $\Gamma$  point, while an isolated nodal ring appears around the M point above the Fermi level. Moreover, it hosts a dispersive nodal loop centered around the K point, appearing as six arcs in the corners of the Brillouin zone. This nodal loop crosses the Fermi level with a considerable dispersion and thus provide an excellent platform to study the fascinating characteristics of dispersive Dirac nodal lines. For the  $\text{AlB}_4$  thin film, on the other hand, three concentric nodal loops were evidenced in the low energy electronic states around the  $\Gamma$  point with hexagon or hexagram momentum distributions. More importantly, we identify the first evidence for the emergence of a set of open 2D nonmagnetic type-II nodal arcs in the  $\text{AlB}_4$  Brillouin zone, linked with a type-I nodal line. The rather large energy dispersion ( $\sim 1.3$  eV) of these Dirac nodal arcs, their coexistence with multiple type-I NLs, and the high-temperature superconducting behavior of  $\text{AlB}_4$  suggest this structure as a distinguished material for advanced research on 2D topological superconductors.

## Methods

All structural and electronic properties are obtained within the Kohn-Sham DFT calculations with the full potential linearized augmented plane wave (LAPW) method as implemented in the computer package

WIEN2k [74]. The generalized gradient approximation (GGA) in the Perdew-Burke-Ernzerhof (PBE) formulation [75, 76] was used for the exchange-correlation functional. The expansion cutoff  $R_{\text{MT}}K_{\text{max}}$  was set to 8, while a  $30 \times 30 \times 1$   $\Gamma$ -centered  $k$  mesh was applied to sample the BZ for self-consistent-field calculations. The crystal structures are fully relaxed with a total energy and force convergence criteria of  $10^{-4}$  Ry and  $10^{-3}$  Ry/a.u., respectively. A vacuum of more than 20 Å was used to minimize the interactions between the neighboring replica of the system. The maximally localized Wannier functions were constructed by employing the Wannier90 package [77]. The Al s, p and B s, p orbitals are chosen as initial projections for WTB model construction.

In order to calculate the phonon spectra, the interatomic force constants were obtained through a supercell approach by using the HIPHIVE [78] package. We used  $10 \times 10 \times 1$  supercells and then generated the reference rattled structures by applying displacements, randomly sampled from a normal distribution with a standard deviation of 0.01 Å. The HIPHIVE package employs VASP [79, 80] for the required DFT calculations, being performed with the projector augmented-wave (PAW) [81] pseudopotentials and PBE exchange-correlation functional. The PAW plane-wave energy cutoff was set to 500 eV. After finding the force constants, the phonon frequencies were calculated using the PHONOPY package [82].

- 
- [1] B. A. Bernevig, T. L. Hughes, and S.-C. Zhang, *Science* **314**, 1757 (2006).
- [2] M. König, S. Wiedmann, C. Brüne, A. Roth, H. Buhmann, L. W. Molenkamp, X.-L. Qi, and S.-C. Zhang, *Science* **318**, 766 (2007).
- [3] L. Fu, C. L. Kane, and E. J. Mele, *Phys. Rev. Lett.* **98**, 106803 (2007).
- [4] J. E. Moore, *Nature* **464**, 194 (2010).
- [5] Z. F. Wang, N. Su, and F. Liu, *Nano Lett.* **13**, 2842 (2013).
- [6] Y. Zhao, Y. Hu, L. Liu, Y. Zhu, and H. Guo, *Nano Lett.* **11**, 2088 (2011).
- [7] A. A. Burkov, M. D. Hook, and L. Balents, *Phys. Rev. B* **84**, 235126 (2011).
- [8] A. A. Burkov, *Nat. Mater.* **15**, 1145 (2016).
- [9] N. P. Armitage, E. J. Mele, and A. Vishwanath, *Rev. Mod. Phys.* **90**, 015001 (2018).
- [10] B.-J. Yang and N. Nagaosa, *Nat. Commun.* **5**, 4898 (2014).
- [11] S. S. Baik, K. S. Kim, Y. Yi, and H. J. Choi, *Nano Lett.* **15**, 7788 (2015).
- [12] X. Wan, A. M. Turner, A. Vishwanath, and S. Y. Savrasov, *Phys. Rev. B* **83**, 205101 (2011).
- [13] S. M. Young, S. Zaheer, J. C. Y. Teo, C. L. Kane, E. J. Mele, and A. M. Rappe, *Phys. Rev. Lett.* **108**, 140405 (2012).
- [14] Z. K. Liu, B. Zhou, Y. Zhang, Z. J. Wang, H. M. Weng, D. Prabhakaran, S.-K. Mo, Z. X. Shen, Z. Fang, X. Dai, Z. Hussain, and Y. L. Chen, *Science* **343**, 864 (2014).
- [15] A. A. Soluyanov, D. Gresch, Z. Wang, Q. Wu, M. Troyer, X. Dai, and B. A. Bernevig, *Nature* **527**, 495 (2015).
- [16] B. Q. Lv, N. Xu, H. M. Weng, J. Z. Ma, P. Richard, X. C. Huang, L. X. Zhao, G. F. Chen, C. E. Matt, F. Bisti, V. N. Strocov, J. Mesot, Z. Fang, X. Dai, T. Qian, M. Shi, and H. Ding, *Nat. Phys.* **11**, 724 (2015).
- [17] S.-Y. Xu, I. Belopolski, N. Alidoust, M. Neupane, G. Bian, C. Zhang, R. Sankar, G. Chang, Z. Yuan, C.-C. Lee, S.-M. Huang, H. Zheng, J. Ma, D. S. Sanchez, B. Wang, A. Bansil, F. Chou, P. P. Shibayev, H. Lin, S. Jia, and M. Z. Hasan, *Science* **349**, 613 (2015).
- [18] Y. Chen, Y. Xie, S. A. Yang, H. Pan, F. Zhang, M. L. Cohen, and S. Zhang, *Nano Lett.* **15**, 6974 (2015).
- [19] Y. Kim, B. J. Wieder, C. L. Kane, and A. M. Rappe, *Phys. Rev. Lett.* **115**, 036806 (2015).
- [20] K. Mullen, B. Uchoa, and D. T. Glatzhofer, *Phys. Rev. Lett.* **115**, 026403 (2015).
- [21] H. Weng, Y. Liang, Q. Xu, R. Yu, Z. Fang, X. Dai, and Y. Kawazoe, *Phys. Rev. B* **92**, 045108 (2015).
- [22] M. Hirayama, R. Okugawa, T. Miyake, and S. Murakami, *Nat. Commun.* **8**, 14022 (2017).
- [23] T. Bzdusek, Q. Wu, A. Ruegg, M. Sigrist, and A. A. Soluyanov, *Nature* **538**, 75 (2016).
- [24] X. Zhang, Z.-M. Yu, X.-L. Sheng, H. Y. Yang, and S. A. Yang, *Phys. Rev. B* **95**, 235116 (2017).
- [25] X. Feng, C. Yue, Z. Song, Q. Wu, and B. Wen, *Phys. Rev. Materials* **2**, 014202 (2018).

- [26] Z. Liu, R. Lou, P. Guo, Q. Wang, S. Sun, C. Li, S. Thirupathiah, A. Fedorov, D. Shen, K. Liu, H. Lei, and S. Wang, *Phys. Rev. X* **8**, 031044 (2018).
- [27] M. Tian, J. Wang, X. Liu, W. Chen, Z. Liu, H. Du, X. Ma, X. Cui, A. Zhao, Q. Shi, Z. Wang, Y. Luo, J. Yang, B. Wang, and J. G. Hou, *Nano Lett.* **20**, 2157 (2020).
- [28] Q.-F. Liang, J. Zhou, R. Yu, Z. Wang, and H. Weng, *Phys. Rev. B* **93**, 085427 (2016).
- [29] C. Zhong, Y. Chen, Y. Xie, S. A. Yang, M. L. Cohen, and S. B. Zhang, *Nanoscale* **8**, 7232 (2016).
- [30] W. Wu, Y. Liu, S. Li, C. Zhong, Z.-M. Yu, X.-L. Sheng, Y. X. Zhao, and S. A. Yang, *Phys. Rev. B* **97**, 115125 (2018).
- [31] Q. Xu, Z. Song, S. Nie, H. Weng, Z. Fang, and X. Dai, *Phys. Rev. B* **92**, 205310 (2015).
- [32] A. Topp, R. Queiroz, A. Grüneis, L. Mühler, A. W. Rost, A. Varykhalov, D. Marchenko, M. Krivenkov, F. Rodolakis, J. L. McChesney, B. V. Lotsch, L. M. Schoop, and C. R. Ast, *Phys. Rev. X* **7**, 041073 (2017).
- [33] B. Wang, H. Gao, Q. Lu, W. Xie, Y. Ge, Y.-H. Zhao, K. Zhang, and Y. Liu, *Phys. Rev. B* **98**, 115164 (2018).
- [34] B.-B. Fu, C.-J. Yi, T.-T. Zhang, M. Caputo, J.-Z. Ma, X. Gao, B. Q. Lv, L.-Y. Kong, Y.-B. Huang, P. Richard, M. Shi, V. N. Strocov, C. Fang, H.-M. Weng, Y.-G. Shi, T. Qian, and H. Ding, *Sci. Adv.* **5** (2019), 10.1126/sciadv.aau6459.
- [35] J.-W. Rhim and Y. B. Kim, *Phys. Rev. B* **92**, 045126 (2015).
- [36] N. B. Kopnin, T. T. Heikkilä, and G. E. Volovik, *Phys. Rev. B* **83**, 220503 (2011).
- [37] Y. Huh, E.-G. Moon, and Y. B. Kim, *Phys. Rev. B* **93**, 035138 (2016).
- [38] P. Zhou, Z. S. Ma, and L. Z. Sun, *J. Mater. Chem. C* **6**, 1206 (2018).
- [39] Y.-J. Jin, R. Wang, J.-Z. Zhao, Y.-P. Du, C.-D. Zheng, L.-Y. Gan, J.-F. Liu, H. Xu, and S. Y. Tong, *Nanoscale* **9**, 13112 (2017).
- [40] S. Li, Y. Liu, S.-S. Wang, Z.-M. Yu, S. Guan, X.-L. Sheng, Y. Yao, and S. A. Yang, *Phys. Rev. B* **97**, 045131 (2018).
- [41] C. Zhong, W. Wu, J. He, G. Ding, Y. Liu, D. Li, S. A. Yang, and G. Zhang, *Nanoscale* **11**, 2468 (2019).
- [42] W. Wu, Y. Jiao, S. Li, X.-L. Sheng, Z.-M. Yu, and S. A. Yang, *Phys. Rev. Materials* **3**, 054203 (2019).
- [43] B. Yang, X. Zhang, and M. Zhao, *Nanoscale* **9**, 8740 (2017).
- [44] H. Feng, C. Liu, S. Zhou, N. Gao, Q. Gao, J. Zhuang, X. Xu, Z. Hu, J. Wang, L. Chen, J. Zhao, S. X. Dou, and Y. Du, *Nano Lett.* **20**, 2537 (2020).
- [45] S. Gupta, A. Kutana, and B. I. Yakobson, *J. Phys. Chem. Lett.* **9**, 2757 (2018).
- [46] J.-L. Lu, W. Luo, X.-Y. Li, S.-Q. Yang, J.-X. Cao, X.-G. Gong, and H.-J. Xiang, *Chinese Phys. Lett.* **34**, 057302 (2017).
- [47] B. Feng, B. Fu, S. Kasamatsu, S. Ito, P. Cheng, C.-C. Liu, Y. Feng, S. Wu, S. K. Mahatha, P. Sheverdyaeva, P. Moras, M. Arita, O. Sugino, T.-C. Chiang, K. Shimada, K. Miyamoto, T. Okuda, K. Wu, L. Chen, Y. Yao, and I. Matsuda, *Nat. Commun.* **8**, 1007 (2017).
- [48] L. Gao, J.-T. Sun, J.-C. Lu, H. Li, K. Qian, S. Zhang, Y.-Y. Zhang, T. Qian, H. Ding, X. Lin, S. Du, and H.-J. Gao, *Adv. Mater.* **30**, 1707055 (2018).
- [49] J. Nagamatsu, N. Nakagawa, T. Muranaka, Y. Zenitani, and J. Akimitsu, *Nature* **410**, 63 (2001).
- [50] V. A. Gasparov, N. Sidorov, I. Zver'Kova, and M. Kurlakov, *Jetp Lett.* **73**, 532 (2001).
- [51] D. Sharma, J. Kumar, A. Vajpayee, R. Kumar, P. K. Ahluwalia, and V. P. S. Awana, *J. Supercond. Nov. Magn.* **24**, 1925 (2011).
- [52] M. Putti, E. Galleani d'Agliano, D. Marrè, F. Napoli, M. Tassisto, P. Manfrinetti, A. Palenzona, C. Rizzuto, and S. Massida, *Eur. Phys. J. B* **25**, 439 (2002).
- [53] R. W. Cumberland, M. B. Weinberger, J. J. Gilman, S. M. Clark, S. H. Tolbert, and R. B. Kaner, *J. Am. Chem. Soc.* **127**, 7264 (2005).
- [54] C.-J. Yi, B. Q. Lv, Q. S. Wu, B.-B. Fu, X. Gao, M. Yang, X.-L. Peng, M. Li, Y.-B. Huang, P. Richard, M. Shi, G. Li, O. V. Yazyev, Y.-G. Shi, T. Qian, and H. Ding, *Phys. Rev. B* **97**, 201107 (2018).
- [55] R. Lou, P. Guo, M. Li, Q. Wang, Z. Liu, S. Sun, C. Li, X. Wu, Z. Wang, Z. Sun, D. Shen, Y. Huang, K. Liu, Z.-Y. Lu, H. Lei, H. Ding, and S. Wang, *npj Quantum Materials* **3**, 43 (2018).
- [56] K.-H. Jin, H. Huang, J.-W. Mei, Z. Liu, L.-K. Lim, and F. Liu, *npj Computational Materials* **5**, 57 (2019).
- [57] D. Takane, S. Souma, K. Nakayama, T. Nakamura, H. Oinuma, K. Hori, K. Horiba, H. Kumigashira, N. Kimura, T. Takahashi, and T. Sato, *Phys. Rev. B* **98**, 041105 (2018).
- [58] M. Humood, J. L. Meyer, S. V. Verkhoturov, T. Ozkan, M. Eller, E. A. Schweikert, J. Economy, and A. A. Polycarpou, *Journal of Materials Research* **33**, 2318 (2018).
- [59] V. Sunko, D. Milosavljević, F. Mazzola, O. J. Clark, U. Burkhardt, T. K. Kim, H. Rosner, Y. Grin, A. P. Mackenzie, and P. D. C. King, *Phys. Rev. B* **102**, 035143 (2020).
- [60] D. Geng, K. Yu, S. Yue, J. Cao, W. Li, D. Ma, C. Cui, M. Arita, S. Kumar, E. F. Schwier, K. Shimada, P. Cheng, L. Chen, K. Wu, Y. Yao, and B. Feng, *Phys. Rev. B* **101**, 161407 (2020).
- [61] G. L. Bir and G. E. Pikus, *Symmetry and strain-induced effects in semiconductors* (Wiley, 1974).
- [62] D. Campi, S. Kumari, and N. Marzari, *Nano Lett.* **21**, 3435 (2021).
- [63] D. B. Litvin and T. R. Wike, *Character Tables and Compatibility Relations of the Eighty Layer Groups and Seventeen Plane Groups* (Springer US, 1991).
- [64] G. F. Koster, J. D. Dimmock, R. G. Wheeler, and H. Statz, *The Properties of the Thirty-Two Point Groups* (M.I.T. Press, 1963).
- [65] F. Geissler, J. C. Budich, and B. Trauzettel, *New Journal of Physics* **15**, 085030 (2013).
- [66] R. Winkler, *Spin-orbit Coupling Effects in Two-Dimensional Electron and Hole Systems*, Springer Tracts in Modern Physics (Springer, Berlin, Heidelberg, 2003).
- [67] C. Herring, *Phys. Rev.* **52**, 361 (1937).
- [68] R. Winkler and U. Zülicke, *Phys. Rev. B* **82**, 245313 (2010).
- [69] Y. Zhao, C. Lian, S. Zeng, Z. Dai, S. Meng, and J. Ni, *Phys. Rev. B* **100**, 094516 (2019).
- [70] Y. Shao, A. N. Rudenko, J. Hu, Z. Sun, Y. Zhu, S. Moon, A. J. Millis, S. Yuan, A. I. Lichtenstein, D. Smirnov, Z. Q. Mao, M. I. Katsnelson, and D. N. Basov, *Nat. Phys.* **16**, 636 (2020).
- [71] Z.-M. Yu, Y. Yao, and S. A. Yang, *Phys. Rev. Lett.* **117**, 077202 (2016).
- [72] M. Udagawa and E. J. Bergholtz, *Phys. Rev. Lett.* **117**,

- 086401 (2016).
- [73] T. E. O'Brien, M. Diez, and C. W. J. Beenakker, *Phys. Rev. Lett.* **116**, 236401 (2016).
- [74] P. Blaha, K. Schwarz, G. K. H. Madsen, D. Kvasnicka, J. Luitz, R. Laskowski, F. Tran, and L. D. Marks, *WIEN2k, An Augmented Plane Wave + Local Orbitals Program for Calculating Crystal Properties* (Karlheinz Schwarz, Techn. Universitat Wien, Austria, 2018).
- [75] J. P. Perdew, K. Burke, and M. Ernzerhof, *Phys. Rev. Lett.* **77**, 3865 (1996).
- [76] P. E. Blöchl, *Phys. Rev. B* **50**, 17953 (1994).
- [77] G. Pizzi, V. Vitale, R. Arita, S. Blügel, F. Freimuth, G. Géranton, M. Gibertini, D. Gresch, C. Johnson, T. Koretsune, J. Ibañez-Azpiroz, H. Lee, J.-M. Lihm, D. Marchand, A. Marrazzo, Y. Mokrousov, J. I. Mustafa, Y. Nohara, Y. Nomura, L. Paulatto, S. Poncé, T. Ponweiser, J. Qiao, F. Thöle, S. S. Tsirkin, M. Wierzbowska, N. Marzari, D. Vanderbilt, I. Souza, A. A. Mostofi, and J. R. Yates, *Journal of Physics: Condensed Matter* **32**, 165902 (2020).
- [78] F. Eriksson, E. Fransson, and P. Erhart, *Advanced Theory and Simulations* **2**, 1800184 (2019).
- [79] G. Kresse and J. Furthmüller, *Phys. Rev. B* **54**, 11169 (1996).
- [80] G. Kresse and J. Furthmüller, *Computational Materials Science* **6**, 15 (1996).
- [81] P. E. Blöchl, *Phys. Rev. B* **50**, 17953 (1994).
- [82] A. Togo and I. Tanaka, *Scripta Materialia* **108**, 1 (2015).
- [83] S. L. Altmann and P. Herzig, *Point-group theory tables* (Clarendon Press, Oxford, 1994).

### Author contributions

S. Abedi and E. Taghizadeh Sisakht contributed equally to this work.

### Conflicts of interest

There are no conflicts to declare.



## SUPPLEMENTARY INFORMATION

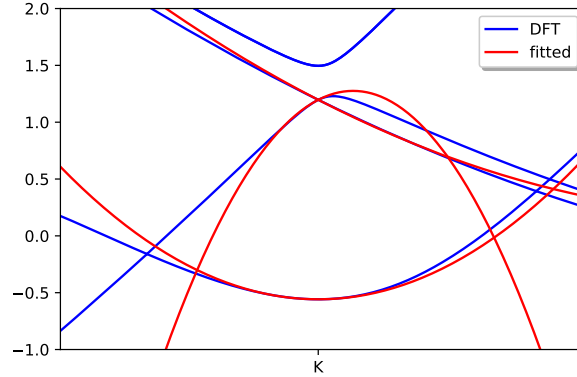
**Supplementary Note 1. Supporting information of the continuum model for  $\text{Al}_2\text{B}_2$  configuration around the K point.**TABLE S1. Symmetrized matrices for the invariant expansion of the diagonal blocks  $\mathcal{H}_{ii}$  for the point group  $D_{3h}$ .

| Block              | Representations                    | Symmetrized matrices            | Tensor components                                  |
|--------------------|------------------------------------|---------------------------------|--|
| $\mathcal{H}_{11}$ | $\Gamma_6 \otimes \Gamma_6^*$      | $\Gamma_1 : \mathbb{1}$         | $\Gamma_1 : 1; k_x^2 + k_y^2$                      |
|                    | $= \Gamma_1 + \Gamma_2 + \Gamma_6$ | $\Gamma_2 : \sigma_z$           | $\Gamma_2 : -$                                     |
|                    |                                    | $\Gamma_6 : \sigma_x, \sigma_y$ | $\Gamma_6 : (k_x, k_y); (k_y^2 - k_x^2, 2k_x k_y)$ |
| $\mathcal{H}_{22}$ | $\Gamma_4 \otimes \Gamma_4^*$      | $\Gamma_1 : \mathbb{1}$         | $\Gamma_1 : 1; k_x^2 + k_y^2$                      |
|                    | $= \Gamma_1$                       |                                 |  |

$$E_{1,2}(k_x, k_y) = E_0 + A(k_x^2 + k_y^2) \pm \sqrt{B^2(k_x^2 + k_y^2) + C^2(k_x^2 + k_y^2)^2 - 2BC(k_x^3 - 3k_x k_y^2)}, \quad (\text{S1})$$

$$E_3(k_x, k_y) = E'_0 + A'(k_x^2 + k_y^2). \quad (\text{S2})$$

The fitted parameters are  $E_0 = 1.19$  eV,  $A = -113.16$  eV $\text{\AA}^2$ ,  $B = 8.78$  eV $\text{\AA}$ ,  $C = 132.10$  eV $\text{\AA}^2$ ,  $E'_0 = -0.56$  eV,  $A' = 66.33$  eV $\text{\AA}^2$ . The fitted bands are shown in Supplementary Fig. S1.

Supplementary Fig S1. Comparison between DFT bands and the bands from the continuum model near the K point of  $\text{Al}_2\text{B}_2$ .

**Supplementary Note 2. Supporting information of the continuum model for  $\text{Al}_2\text{B}_2$  configuration around the  $\Gamma$  point.**

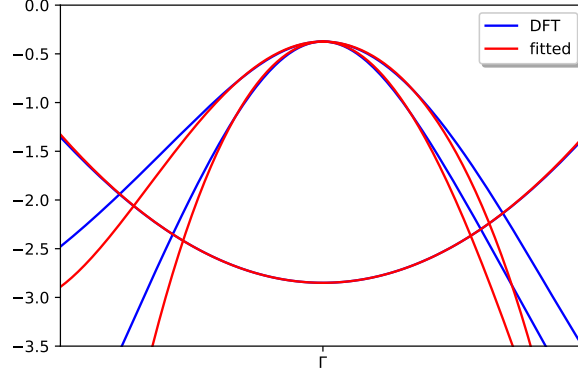
TABLE S2. Symmetrized matrices for the invariant expansion of the diagonal blocks  $\mathcal{H}_{ii}$  for the point group  $D_{6h}$ .

| Block              | Representations                                      | Symmetrized matrices              | Tensor components   |
|--------------------|--|-----------------------------------|---|
| $\mathcal{H}_{11}$ | $\Gamma_6^+ \otimes \Gamma_6^{+*}$                   | $\Gamma_1^+ : \mathbf{1}$         | $\Gamma_1^+ : 1; k_x^2 + k_y^2$   |
|                    | $= \Gamma_1^+ + \Gamma_2^+ + \Gamma_6^+$             | $\Gamma_2^+ : \sigma_z$           | $\Gamma_2^+ : -$  |
|                    |  | $\Gamma_6^+ : \sigma_x, \sigma_y$ | $\Gamma_6^+ : (k_y^2 - k_x^2, 2k_x k_y); (k_x^4 - 6k_x^2 k_y^2 + k_y^4, 4k_x k_y^3 + 4k_x^3 k_y)$ |
| $\mathcal{H}_{22}$ | $\Gamma_2^- \otimes \Gamma_2^{-*}$<br>$= \Gamma_1^+$ | $\Gamma_1^+ : \mathbf{1}$         | $\Gamma_1^+ : 1; k_x^2 + k_y^2$   |

$$E_{1,2}(k_x, k_y) = E_0 + A(k_x^2 + k_y^2) \pm \sqrt{B^2(k_x^2 + k_y^2)^2 + C^2(k_x^2 + k_y^2)^4 - 2BC(k_x^6 - 15k_x^4 k_y^2 + 15k_x^2 k_y^4 - k_y^6)}, \quad (\text{S3})$$

$$E_3(k_x, k_y) = E'_0 + A'(k_x^2 + k_y^2). \quad (\text{S4})$$

The fitted parameters are  $E_0 = -0.37$  eV,  $A = -43.88$  eV $\text{\AA}^2$ ,  $B = 11.10$  eV $\text{\AA}^4$ ,  $C = 100.17$  eV $\text{\AA}^4$ ,  $E'_0 = -2.85$  eV,  $A' = 12.36$  eV $\text{\AA}^2$ . The fitted bands are shown in Supplementary Fig. S2.



Supplementary Fig S2. Comparison between DFT bands and the bands from the continuum model near the  $\Gamma$  point of  $\text{Al}_2\text{B}_2$ .

**Supplementary Note 3. Supporting information of the continuum model for  $\text{AlB}_4$  configuration around the  $\Gamma$  point.**

TABLE S3. Symmetrized matrices for the invariant expansion of the diagonal blocks  $\mathcal{H}_{ii}$  for the point group  $D_{6h}$ .

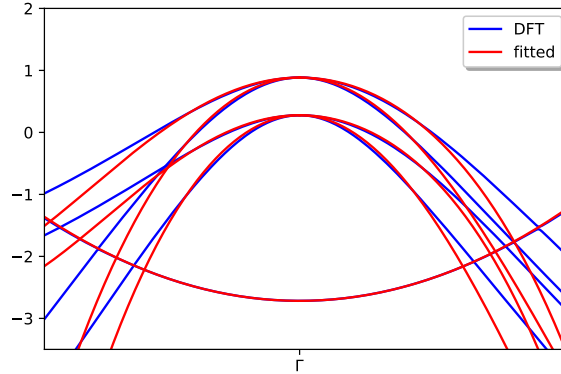
| Block              | Representations                          | Symmetrized matrices              | Tensor components   |
|--------------------|--|-----------------------------------|---|
| $\mathcal{H}_{11}$ | $\Gamma_6^- \otimes \Gamma_6^{-*}$       | $\Gamma_1^+ : \mathbf{1}$         | $\Gamma_1^+ : 1; k_x^2 + k_y^2$   |
|                    | $= \Gamma_1^+ + \Gamma_2^+ + \Gamma_6^+$ | $\Gamma_2^+ : \sigma_z$           | $\Gamma_2^+ : -$  |
|                    |  | $\Gamma_6^+ : \sigma_x, \sigma_y$ | $\Gamma_6^+ : (k_y^2 - k_x^2, 2k_x k_y); (k_x^4 - 6k_x^2 k_y^2 + k_y^4, 4k_x k_y^3 + 4k_x^3 k_y)$ |
| $\mathcal{H}_{22}$ | $\Gamma_6^+ \otimes \Gamma_6^{+*}$       | $\Gamma_1^+ : \mathbf{1}$         | $\Gamma_1^+ : 1; k_x^2 + k_y^2$   |
|                    | $= \Gamma_1^+ + \Gamma_2^+ + \Gamma_6^+$ | $\Gamma_2^+ : \sigma_z$           | $\Gamma_2^+ : -$  |
|                    |  | $\Gamma_6^+ : \sigma_x, \sigma_y$ | $\Gamma_6^+ : (k_y^2 - k_x^2, 2k_x k_y); (k_x^4 - 6k_x^2 k_y^2 + k_y^4, 4k_x k_y^3 + 4k_x^3 k_y)$ |
| $\mathcal{H}_{33}$ | $\Gamma_2^- \otimes \Gamma_2^{-*}$       | $\Gamma_1^+ : \mathbf{1}$         | $\Gamma_1^+ : 1; k_x^2 + k_y^2$   |
|                    | $= \Gamma_1^+$                           |                                   |   |

$$E_{1,2}(k_x, k_y) = E_0 + A(k_x^2 + k_y^2) \pm \sqrt{B^2(k_x^2 + k_y^2)^2 + C^2(k_x^2 + k_y^2)^4 - 2BC(k_x^6 - 15k_x^4 k_y^2 + 15k_x^2 k_y^4 - k_y^6)}, \quad (\text{S5})$$

$$E_{3,4}(k_x, k_y) = E'_0 + A'(k_x^2 + k_y^2) \pm \sqrt{B'^2(k_x^2 + k_y^2)^2 + C'^2(k_x^2 + k_y^2)^4 - 2B'C'(k_x^6 - 15k_x^4 k_y^2 + 15k_x^2 k_y^4 - k_y^6)}, \quad (\text{S6})$$

$$E_5(k_x, k_y) = E''_0 + A''(k_x^2 + k_y^2). \quad (\text{S7})$$

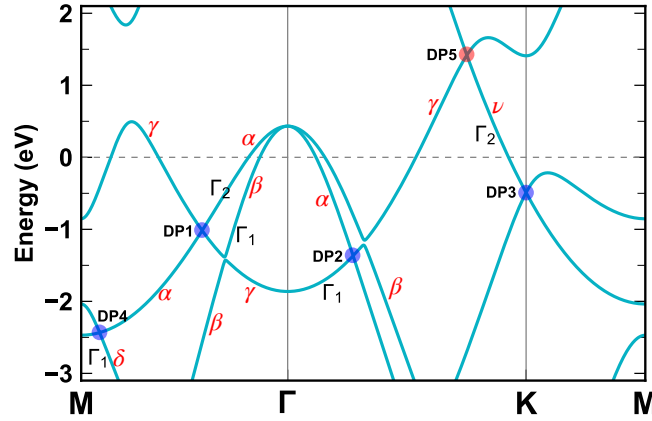
The fitted parameters are  $E_0 = 0.28$  eV,  $A = -42.10$  eV $\text{\AA}^2$ ,  $B = 12.55$  eV $\text{\AA}^2$ ,  $C = 74.19$ eV $\text{\AA}^4$ ,  $E'_0 = 0.88$  eV,  $A' = -36.14$  eV $\text{\AA}^2$ ,  $B' = 8.80$  eV $\text{\AA}^2$ ,  $C' = 58.35$ eV $\text{\AA}^4$ ,  $E''_0 = -2.72$  eV,  $A'' = 11.64$  eV $\text{\AA}^2$ . The fitted bands are shown in Supplementary Fig. S3.



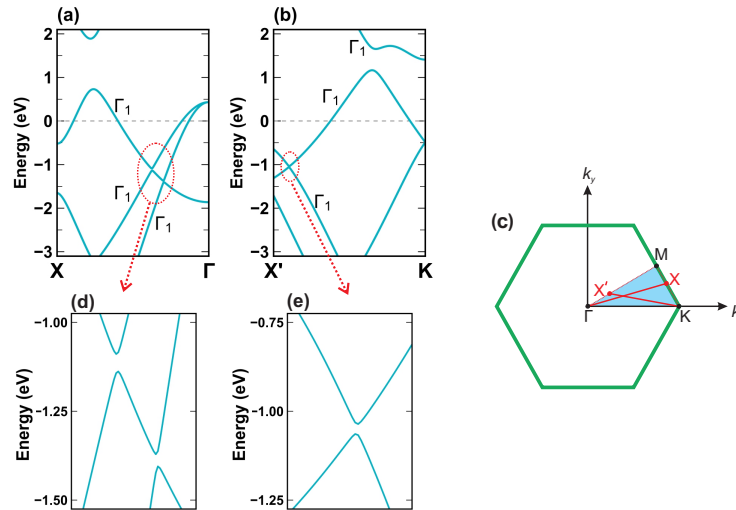
Supplementary Fig S3. Comparison between DFT bands and the bands from the continuum model near the  $\Gamma$  point of  $\text{AlB}_4$ .

### Supplementary Note 4. Electronic properties of monolayer AlB<sub>2</sub>.

The electronic band structure of freestanding monolayer AlB<sub>2</sub> is shown in Fig. S4. Within 2.5 eV of the Fermi level there are several bands which cross to each other to form four  $p$ -type Dirac cones below (red circles) and a gapless  $n$ -type Dirac cone above (blue circle) the Fermi surface, respectively. We mark these bands by Greek letters as shown in the Figure. Group theory analysis of these energy bands shows that along the  $\Gamma$ -M and K-M symmetry directions the small groups are  $C_s$  which has an out of plane symmetry element. Along these directions  $\beta$ ,  $\gamma$  and  $\delta$  bands belong to the  $\Gamma_1$  IR which have positive mirror parity. Also, the IR of  $\alpha$  and  $\nu$  bands are  $\Gamma_2$  with a negative mirror eigenvalue [83]. As a result, within the mentioned energy window one can observe the formation of four Dirac points DP1-DP4 due to the crossing of bands with opposite mirror parities. The remained Dirac point (DP3) is located at the K point which arises from the boron hexagonal lattice as the Dirac's cones of graphene. Note that due to the absence of in-plane mirror symmetry in monolayer AlB<sub>2</sub>, along arbitrary low-symmetry directions X- $\Gamma$  and X'-K one can see no crossing feature (see Figs. S5(a) and (b)). Therefore, we do not expect to observe symmetry protected nodal lines in this structure. The existence of the  $p$ -type Dirac Fermions in this configuration has been confirmed by recent experimental ARPES measurements [60] which provides an excellent platform for designing new nanoelectronics.



Supplementary Fig S4. The electronic band structure of monolayer AlB<sub>2</sub> along the high symmetry paths M- $\Gamma$ -K-M. The  $p$ - and  $n$ -type Dirac cones are shown by red and blue circles, respectively.



Supplementary Fig S5. The electronic band structure of monolayer AlB<sub>2</sub> along typical low-symmetry directions (a) X- $\Gamma$  and (b) X'-K as shown in (c). The zoomed-in band structures in the red ellipses are shown in (d) and (e).